F autoradiography with the Mimosa-28: Characterisation and Application

Pham Nguyen Truong, Patrice Marchand, Christian Finck, Frédéric Boisson, David Boisson, David Brasse, Patrice Laquerriere

^{18}F autoradiography with the Mimosa-28: Characterisation and Application

Truong Nguyen Pham, Patrice Marchand, Christian Finck, Frédéric Boisson, David Brasse and Patrice Laquerriere
Université de Strasbourg, CNRS, IPHC, UMR 7178, F-67000 Strasbourg, France
E-mail: patrice.laquerriere@iphc.cnrs.fr

***Abstract*—Autoradiography is a technique used to record the spatial distribution of a radiotracer into an ex-vivo tissue slice. Within the section, the radioactive molecules emit charged particles from specific binding sites. These particles pass through the tissue before being detected by a sensor. Autoradiography gives the distribution of a radioactive molecule with a spatial resolution of approximately one hundred microns. In this work, we investigated the feasibility of autoradiography with a CMOS-APS sensor using radioactive isotope ^{18}F. This sensor works in digital mode by collecting charges. It presents a linear response with isotope ^{18}F for activity between 1 kBq and 1 MBq. The detection efficiency is 44,0 $\pm$ 0,5% for this range of activity with a spatial resolution of 144 $\pm$ 3 μm by using the absorber edge method. The Mimosa-28 sensor performs autoradiography imaging with a rose leaf and a mouse brain section which has a thickness of 50 μm and an activity of 4 kBq in the slice.**

***Keywords*—Autoradiography, CMOS APS, fluorine 18, brain**

I. Introduction

Molecular imaging like PET (Positron Emission Tomography) scan gives the possibility to study, *in vivo*, a biological process within a body using a radiolabelled molecule .PET scan has the best sensitivity (around a few picomoles) [1]. One limitation of a PET scan is its relatively low spatial resolution (currently around 1 mm for preclinical systems). This resolution limits us to study the heterogeneity of the biodistribution at the tissue scale. Autoradiography (AR) offers the possibility, in particular conditions (section thickness, exposure time), to obtain the distribution of the radiotracer in the organ with a better spatial resolution (some micrometers) with an excellent sensitivity. In 1904, London presented biological autoradiography for the first time using radium [2]. Today AR has many uses to examine the distribution of antibodies in a tumor of a mouse [3], the distribution of different radiotracer on histology sections of myocardial infarction [4], the distribution of glucose in the mouse brain under conscious and isoflurane-anaesthetised conditions [5]. Due to its long exposure time and in order to obtain a better spatial resolution, AR images are obtained ex-vivo on tissue sections. To examine the capability of the Mimosa-28 to perform AR using charged particles, we evaluate its characteristics: spatial resolution, linearity, efficiency using fluorine 18. It is essential to have the best spatial resolution, a high sensitivity to the charged particles emitted from the radiotracer to reduce the acquisition time and/or have an excellent signal to noise ratio, excellent counting linearity to have a high useful range. Finally, the detection surface must be as wide as the section that is being imaged.

The emulsion film is an often-used technique in AR because the technique is inexpensive and gives an intrinsic spatial resolution of 3.5 μm depending on the size of silver halide crystals, 0,1 - 0,4 μm in diameter [6] [7]. Nonetheless, this technique has some limitations [8][9]: it has poor linearity, a short dynamic range depending on the activity and low sensitivity. Consequently, the exposure time must be longer which can take from several days to months if the half-life of the isotope authorizes.

The phosphor plate has also been used to perform AR [10][5]. This imaging technique presents good linearity and a wide dynamic range (characteristics are reported in table 1) [11].

The gaseous triethylamine scintillation detector with 2 parallel plates, a cathode and an anode, can also be used to perform AR [12]. This system presents a 100% efficiency with beta particles and a spatial resolution of 150 μm for ^{18}F [13].

A scintillating layer can be employed to detect the particles emitted from the tissue section [4].

CCD (Charge Coupled Device) can perform AR application. The CCD sensor with direct detection ([14], [15]) and indirect detection coupled with a scintillating layer ([4], [13]) or a microscope [16] have been used to image the distribution of β^+ emitters from the tissue. An ultrathin phosphor plate with a thickness of 3 μm coupled with a CCD camera can be used to quantify the distribution of FDG [17].

Silicon-based pixel detectors CMOS (Complementary Metal Oxide Semiconductor) have been used to do AR. The Medipix2 detector used a centroid reconstruction of the cluster [18]. The Timepix [19] has been used to image the distribution of FDG in the 20 μm section of heart [20].

The CCD sensor has been used in comparison with the CMOS-APS (active pixel sensor) sensor and the film [15]. ^{3}H and ^{14}C have been used to compare the linearity and the efficiency between CCD and CMOS and their AR application. CCD and CMOS has equivalent performance and can perform AR.

All these techniques are summarized in table I with the use of ^{18}F. Linearity, dynamic range, spatial resolution and counting efficiency are the parameters needed to perform appropriately AR.

Physicists have used the CMOS-APS in high energy physics as a tracker. The spatial resolution of Mimosa-28 can achieve 4 μm with an efficiency close to 100% [21]. In this article,

TABLE I: Performance of different systems used for AR of the brain slice with ^{18}F.

Technique	Dynamic range (decades)	Spatial resolution (μm)	Efficiency (counts/s/Bq)	Surface (cm^2)
Film [6]	2	intrinsic 3.5	-	variable
Phosphor plate [11]	4	330 $\pm$ 24	0,5	12,7 x 12,7
Phosphor with CCD [17]	4	69	0,01	2,5 x 2,5
CCD [14]	3	$\simeq$ 35	0,084	1,73 x 2,59
Scintillating sheet [4]	4	20	-	2,4 x 3,2
Gaseous [13]	4	150	-	20 x 25
CMOS [18] [19] [20]	>5	230 $\pm$ 6 Medipix2 132,3 $\pm$ 3,5 Timepix	0,38	1,4 x 1,4

we aim to demonstrate if we can use this sensor with ^{18}F and obtain the same characteristics to perform AR. For this purpose, we measured the counting efficiency, the linearity, the spatial resolution in function of its resistivity. We demonstrate the feasibility using biological samples (rose leaf and mouse brain section).

II. Materials and methods

A. Detector description

The Mimosa-28 is a CMOS active pixel sensor (APS) Fig 1. The PICSEL (Physics with Integrated Cmos Sensors and ELectron machines) group developed it at IPHC. This sensor has been used as a particles tracker in the STAR HFT experiment [21]. It works in digital mode by collecting charges. The spatial resolution is 4 μm with a 100 % efficiency with pions at 120 GeV. The sensor presents two types of resistivity in the epitaxial layer: a high-resistivity of 400 Ωcm and a low-resistivity of 10 Ωcm. The surface of detection is circa 3,8 cm^2 with a 960 x 928 array of pixels on a 20,7 μm pitch with a sensitive field free region of 15 μm. The integration time is 185,6 μs. According to the Beer-Lambert law, a 511 keV photon has 0,0283% probability to interact with the epitaxial layer. Therefore the 511 keV photons had no impact on our measurements. We summarise the characteristics of the Mimosa-28 in table II.

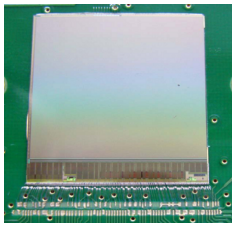

Fig. 1: Picture of the Mimosa-28 sensor (1.9 x 1.9 cm^2) on PCB [21].

The incident particle interacts into the sensitive layer, and the multiple scatterings change the trajectory of the particle in the detector. Along the trajectory, the positron partially gives energy which ionised the sensitive layer by creating a electron-hole pair. This partial energy loss depends on the kinetic energy of the particle and the media. The linear energy transfer (LET) for 600 keV and 250 keV positrons is 366,7 eV/ μm and 480 eV/ μm respectively into silicon [22]. Next, the created electrons drift thermally through the sensitive layer and are collected by the pixel. The created charges are shared by several pixels in the proximity of the trajectory and the charge-sharing effect activated pixels which created a cluster.

The signal received by the pixel is then amplified and registered. This configuration enables the pixel to collect other charges during the acquisition. The system transfers the previous signal to a discriminator where the user imposes a threshold of the pixel. If the signal exceeds this threshold, the output is 1. If not, the output is 0. For each integration time, the computer stores a 960 x 928 matrix that contains the output. At 20 ^oC, 15 electrons approximately activate the pixel in a dark chamber. These 15 electrons represent the threshold 1σ.

B. Centroid determination

A cluster is defined as a group of pixels that were fired from the same particle. The use of algorithm was implemented based on first neighbor search in an iterative way. Hits are considered to belong to a cluster as long as they have a common edge. The centroid is defined as the center of gravity of the all the hits in the cluster. A program coded in C++ using ROOT library is used to reconstruct the centroid of the different clusters [23]. For each integration time, the program reads the 960 x 928 matrix and saves the different clusters found in memory. Since we do not have access to the deposited energy, only the fired pixels are used. For each cluster, the program determines the centroid of the cluster and saves its position in a 960 x 928 histogram.

C. Radiotracer

The ^{18}F is the most common radioisotope used in the PET scan. This isotope is used in all our experiments. ^{18}F is produced on the Cyrcé platform (CNRS/IN2P3 IBISA) via ^{18}O(p, n)^{18}F process. ^{18}F decays by emitting a β^+ (96,86%) and by electron capture (3,14%) [24]. The half-life is 109.8 min. AllinOne (Trasis) synthesizer module performs the radiochemical synthesis of ^{18}F-FDG using the method described [25].

The liberated positron has a continuous energy spectrum extended to 634 keV [26]. The range of the positrons in

TABLE II: Characteristics of the Mimosa-28.

	Surface of detection (cm^2)	Pixel number	Pixel pitch (μm)	Epitaxial layer (μm)	Frame rate (μs)	γ 511 keV interaction (%)
Mimosa-28	3.8	928 x 960	20.7	15	185.6	0.023

water and silicon, shown in table III, is obtained from ICRU (International Commission on Radiation Units and Measurements) data by using the CSDA (Continuous-Slowing-Down Approximation) range ($g.cm^{-2}$) [22].

D. Experimental setup

The experimental setup has already been described ref [27] :

1) Noise measurement: To determine the background in the dark chamber, the sensor acquired during 30 min with different detection threshold σ and the resistivity of the field free layer (at room temperature).

2) Linearity and counting efficiency: To characterize the linearity and the counting efficiency of the sensor, a 5,5 mm in diameter disk of paper was used. The paper contained a solution of ^{18}F-FDG. Then, the disk was put on the surface with a known activity between 1 kBq and 1 MBq measured with a dose calibrator Isomed 2000 with an error of 5 %. The surface of the sensor was covered with a 7 μm thick layer of cellophane film.

The event rate (counts/s) was evaluated by taking the number of reconstructed clusters in the image divided by the exposure time 1,856 s. The event rate was plotted as a function of the source activity normalized by the branching ratio of the ^{18}F. The slope of the simple linear regression designated the efficiency of the detector. We measured the linearity and the counting efficiency of both sensors (low-resistivity layer and high-resistivity).

3) Spatial resolution: The absorbing edge method was adopted to get the spatial resolution [20][28][29][30]. A mask of tungsten with a 1mm thickness was put on the detection surface, protected by a cellophane film, to shield the detector from the β^+ particles, Fig.2. With the high density of the tungsten, the maximum range of a positron emitted by ^{18}F was 0.1 mm [31]. The solution of ^{18}F was placed between 2 coverslips to have a homogeneous distribution. The thickness of the coverslip was 160 μm. This thickness attenuates 67% of 600 keV positrons [32]. The height between the source and the sensor varied between 1 mm and 30 mm to evaluate its impact on the spatial resolution.

The activity concentration was approximately 1 MBq in 5 μL and the acquisition time was 1h for each height. The tool ROOT/C++ was employed to analyze our images and to region of interest that we projected on the x-axis. This treatment gave us a 1D plot of the transition between the two different areas (with or without tungsten attenuation). We obtained the Edge Response Function (ERF) by fitting the 1D plot with the equation (1). The derivative of ERF function gives the Line Spread Function (LSF). Nevertheless, in the function (1), we directly obtained the standard deviation s value to calculate the FWHM of the line spread function. The spatial resolution was measured using a threshold of 12σ and with both resistivities.

$$ERF(x) = \frac{1}{2}\left(1 + \text{erf}\left(\frac{x-\mu}{s\sqrt{2}}\right)\right) \quad (1)$$

where μ (mean) and s (standard deviation) were the parameters of the Gaussian function.

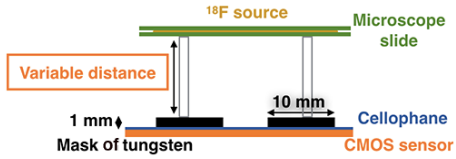

Fig. 2: Scheme of the experimental setup for spatial resolution determination. The source ^{18}F (yellow) was located between 2 coverslips.

4) Ex-vivo tissue imaging preparation: To test Mimosa-28 to perform AR, a rose bush leaf sample with an estimated thickness of 100 μm was used [33]. The stem of the leaf was plunged in a solution of water containing ^{18}F (500 MBq/mL). After 2 hours of uptake, we measured in the leaf 3,2 MBq by using Isomed2000 counter. The leaf was then put on the sensor for 1 hour. The leaf was also imaged with SteREO Discovery V12 with a Zeiss Achromat S 1.25x lens to obtain the optical image. To perform autoradiography imaging, we used the high-resistivity layer and a threshold of 12σ to decrease the noise.

The animal experimentation was approved by the Minister and Institutional Guidelines C.R.E.M.E.A.S (Strasbourg), referral number **2943**. For the ex-vivo brain imaging, the mouse was food-deprived during 4 hours before the injection. The activity concentration of ^{18}F-FDG was 215 MBq/mL and the mouse weighing 53,4 g was injected with a volume of 180 μL by intraperitoneal injection. The mouse was sacrificed 1h later, and the brain was extracted. We measured 477 kBq in the brain of 520,4 mg. To preserve the brain, the brain was embedded by agarose gel 4% (4g in 100mL of water). We obtained the brain slice 50 μm of thickness using a vibratome Leica VT1200S at around 4C^o. An optical image of each block face was recorded during the sectioning process using a Canon EOS 700D with a 100 mm macro lens. We laid the section on the coverslip (24 x 60 x 0,16 mm), and a droplet of oil was put on the tissue to avoid the dryness during the acquisition. Subsequently, the system was placed directly in contact with the sensor. The exposure time was nearly 5 hours. A rigid registration allowed alignment and to fuse the functional AR image from the Mimosa-28 with the optical image [34].

TABLE III: Range of the positrons emitted from ^{18}F.

Energy (keV)	Water	Silicon
	Range (μm)	
249.5	620	333
633.9	2256	1200

5) Signal-to-noise ratio: In the brain slice image, we selected 3 different regions of interest (ROI) where we measured the signal, 2 in the brain and 1 out of the brain (background) areas to calculate the signal-to-noise ratio (SNR) and the image contrast (C):

$$SNR = \frac{m_{ROI}}{s_{background}} \quad (2)$$

$$C = \frac{m_{ROI} - m_{background}}{m_{ROI} + m_{background}} \quad (3)$$

where m and s are the mean signals and the standard deviation respectively in different regions.

III. Results

A. Background noise

During 30 minutes of acquisition, with the low-resistivity epitaxial layer, the sensor recorded an average (5,4 $\pm$ 0.1) 10^{-2} counts/s/mm^2 on the surface of the detector with a threshold of 12σ. With the high-resistivity layer, the noise was (5,0 $\pm$ 0.2) 10^{-4} counts/s/mm^2. We reported the number of events as a function of the threshold in the Fig.3 with the different resistivity layers. Since the noise was very low with this value, we used it in the rest of this article.

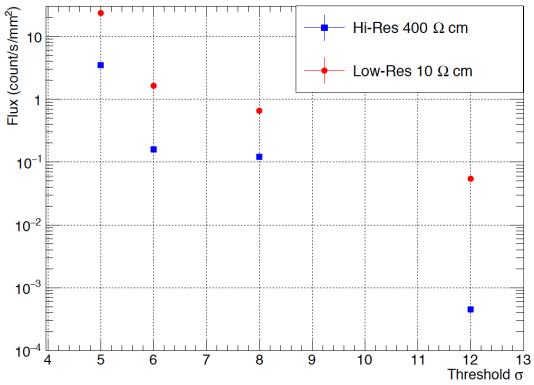

Fig. 3: Variation of the flux as a function of the threshold σ without any radio-activity.

B. Linearity efficiency and dynamic range

Between 1 kBq and 1 MBq, the event rate was linear as a function of the activity. Using the low-resistivity sensor, the efficiency was 39,0 $\pm$ 0,7 % (0,39 counts/s/Bq) with a threshold of 12σ, and the dynamic range had five orders of magnitude. Using high-resistivity sensor, the efficiency was linear with a threshold of 12σ between 1 kBq and 500 kBq. The efficiency was 44,0 $\pm$ 0,5 %, Fig.4. The figure 4 is zoomed on the range 0 to 80kBq.

C. Spatial resolution

With the low-resistivity layer and a threshold of 12σ, the FWMH was 165 $\pm$ 4 μm at 30 mm and 144 $\pm$ 3 μm at 21 mm. With the high-resistivity layer, we obtained 161 $\pm$ 6 μm at 30 mm and 145 $\pm$ 4 μm at 21 mm. At 1 mm distance between the source and the sensor, a difference was observed between the resolution obtained with a high-resistivity sensor and a low-resistivity sensor. At a distance beyond 5 mm, the spatial resolutions were the same for both resistivities. In any case, the spatial resolution was improved (between 10% and 30%) using the centroid determination Fig. 6.

D. Autoradiography imaging

1) Rose leaf sample: We obtained the image 1h after exposure, Fig.7(a). A fusion between the optical image and autoradiography combined the information concerning the distribution and the structure of the leaf, Fig.7(b). We observed an uptake of the solution containing ^{18}F in the primary veins of the leaf.

2) Brain section: Using the Mimosa-28, we obtained the image of the brain slice, 50 μm in thickness, Fig 8. The brain section contained an estimated activity of 4 kBq. A fusion between autoradiography and optical image provided the visualization of the uptake in the different parts of the brain slice.

In the Fig.8(b), we selected 3 ROI of 500 x 350 μm^2: one background outside the brain section, one in the lateral ventricle and one in anterior commissure. In the Fig.9(a), the SNR became constant (SNR = 57) after 200 minutes. The behavior was the same with the contrast, Fig.9(b).

IV. Discussion

A. Efficiency

Our experiments aim to characterize the sensor with ^{18}F. According to our experiments, the efficiencies are 39% and 44% with the low-resistivity layer and the high-resistivity layer respectively. We detected nearby half of the β^+ emitted due to the solid angle, lower than 2π sr. Furthermore, the positrons may be back-scattered or are absorbed by the cellophane and the dead parts of the detector before being detected by the sensor. With a 7 μm thick cellophane film, we lose 3% of efficiency with the source of ^{18}F [19]. The energy spectrum of the β^+ particles from the ^{18}F varies from 0 to 650 keV. Positrons with kinetic energy less than 20 keV represent 2% in the energy spectrum of the beta particles emitted by the ^{18}F. According to the equation in [31], the range is 3 μm for a charged particle with 20 keV in the silicon. Therefore, the dead layer can absorb these 2% positrons before interacting with the sensor.

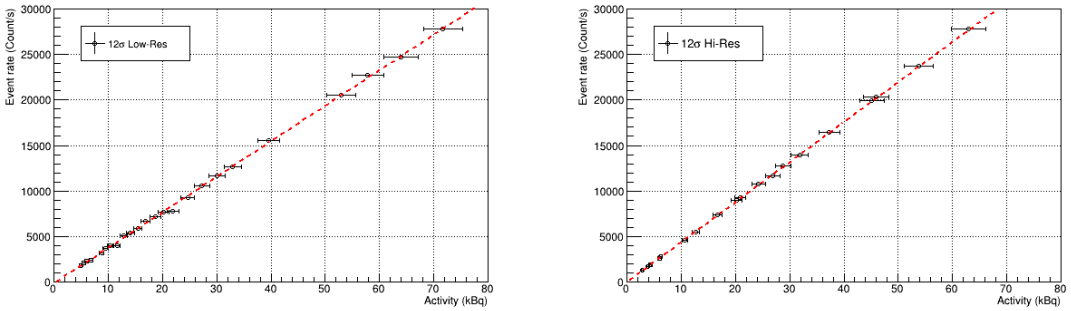

(a) (b)

Fig. 4: Variation of the event rate (counts/s) as a function of the activity of the ^{18}F in the paper with (a) the low-resistivity and (b) the high-resistivity layer with the threshold of 12σ. Event rate is calculated as the number of hit over the full image divided by the exposure time (10000 frames = 1,856s). A linear fit is plotted on the graph.

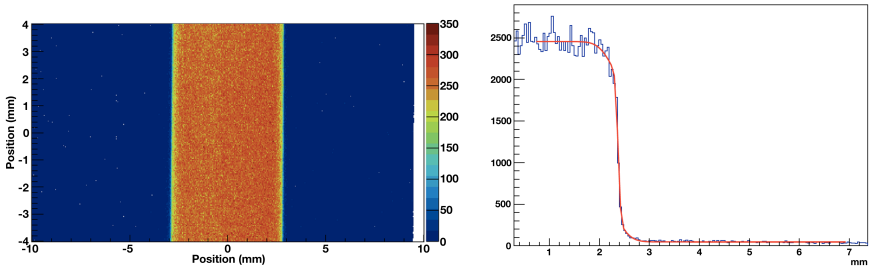

(a) (b)

Fig. 5: (a) Image of ^{18}F activity projected on the sensor with the tungsten mask. Exposure time = 1 hour. The color bar represents the number of hits per pixel. The height is 30 mm between the source and the sensor. (b) Projection of the image on x-axis, fitting of the data (red line).

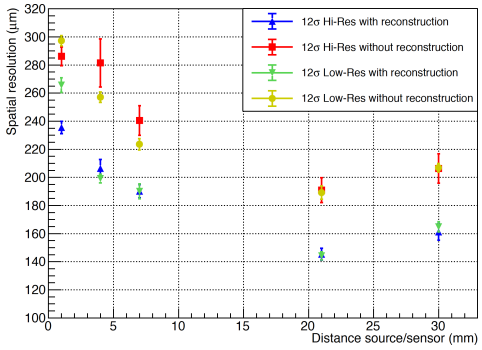

Fig. 6: Spatial resolution as a function of the height between the source and the sensor with the different parameters (with or without centroid determination).

Finally, according to [11], there is self-absorption of the β^+ particles with low energy in the source. The deeper β^+ particles are attenuated in the source, and their contribution to the signal is less than the particles at the surface of the source.

B. *Spatial resolution*

The absorbing edge method is initially used to measure the spatial resolution with a parallel particle beam. The mask stops the particles, and the method gives a clean sharp function. There are several explanations why we did not obtain an ideal edge function. In our case, the emission of positrons is isotropic, and the diffusion effects degrade the measurement of the spatial resolution. Back-scattering effects at the edges of the masks degrade the spatial resolution. In addition, the tungsten layer produces secondary electrons from the Compton effect and the photoelectric absorption induced by 511 keV photons. These electrons add a signal into the sensor under the tungsten. We decrease the degradation of the spatial resolution when we increased the distance between source and sensor. In this case, only positrons with high kinetic energy and perpendicular to the surface of the sensor did interact with the sensor. For positrons highly diffused, the masks plays a role of collimator.

The spatial resolution we obtained is similar to the one of Timepix [19], but the counting efficiency is 44% compared to 38% using Timepix. In general, the characterization of detectors for autoradiography do not follow a general method contrary to the PET scan which has the NEMA standard to

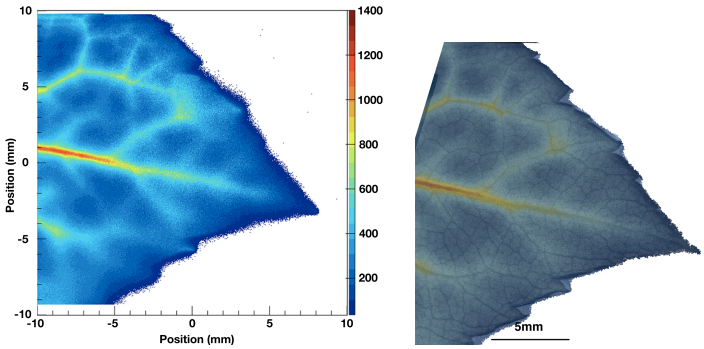

(a) (b)

Fig. 7: (a) Autoradiography of a rose leaf with an uptake of ^{18}F. Exposure time = 1h. (b) Fusion between autoradiography and image from SteREO Discovery.

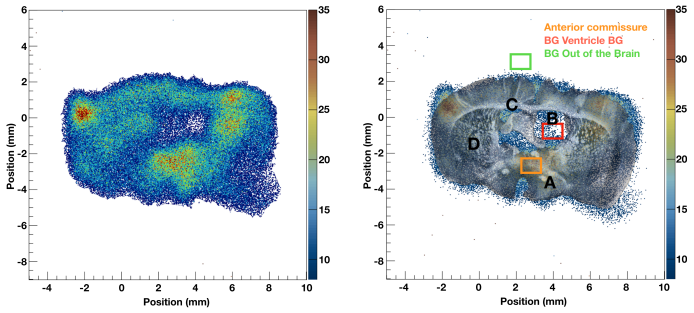

(a) (b)

Fig. 8: (a) Autoradiography of the brain slice with a thickness of 50 μm with the exposure time 4.8 hours. The color bar represents the number of clusters per pixel. The threshold is 5 to 35 hits/pixel. (b) Fusion between autoradiography and photography with the area where we calculate the mean μ and the standard deviation σ. A: anterior commissure, B: lateral ventricle, C: corpus callosum, D: caudate putamen.

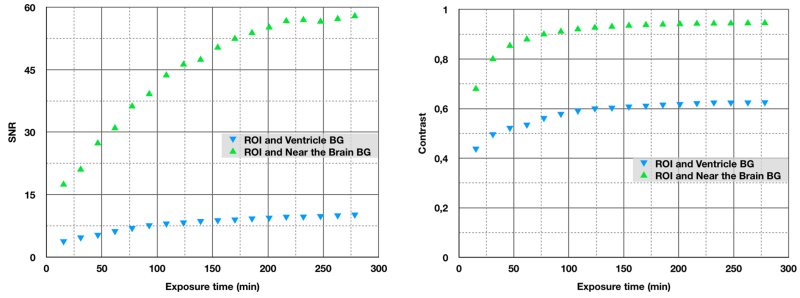

(a) (b)

Fig. 9: (a) SNR of ROI with the different backgrounds as a function of the exposure time. (b) Contrast between the ROI and the backgrounds as a function of the exposure time.

compare two systems in the same conditions. In fact, in autoradiography, each author characterize the sensor differently, and it is extremely difficult to compare results like the spatial resolution, the linearity and the efficiency between 2 detectors for autoradiography. Additionally, some authors characterize the sensor with one isotope and perform autoradiography with another isotope.

V. Conclusion

The Mimosa-28 sensor presents linearity of the signal between 1 MBq and 1 kBq. The spatial resolution is 144 $\pm$ 3 μm at 21 mm distance with the low-resistivity layer and a

threshold of 12σ and 145 ± 4 μm with the high-resistivity layer. Images have been recorded using ^{18}F and a rose bush leaf sample or brain slice. We summarize the characteristics in table IV. The sensor presents the characteristics favorably with state-of-the-art detectors for digital AR. This sensor can image the distribution of ^{18}F-FDG in a tissue section with the AR technique.

TABLE IV: Characteristic of the Mimosa-28 according to the methods with ^{18}F.

Technique AR	Dynamic range (decades)	Optimal spatial resolution (μm)	Efficiency (counts/s/Bq)
Mimosa-28	>5	144 ± 3	$0{,}39 \pm 0{,}07$ for Low-Res $0{,}44 \pm 0{,}05$ for Hi-Res

ACKNOWLEDGMENT

We thank the PICSEL Group for providing technical support and Jean-Daniel Fauny at IBMC for the image of the rose bush leaf. We thank Lionel Thomas and Bruno Jessel for for providing the mouse, Karen Dent for english correction and finally, the MI-CNRS Imag'In for financial support.

REFERENCES

[1] S. R. Cherry, T. Jones, J. S. Karp, J. Qi, W. W. Moses, and R. D. Badawi, "Total-body PET: maximizing sensitivity to create new opportunities for clinical research and patient care," *Journal of Nuclear Medicine*, vol. 59, no. 1, pp. 3–12, 2018.

[2] E. S. London, *Etudes sur la valeur physiologique et pathologique de l'émanation du radium*. Bureaux des Archives d'Électricité Médicale, 1904.

[3] T. Bäck and L. Jacobsson, "The α-camera: a quantitative digital autoradiography technique using a charge-coupled device for ex vivo high-resolution bioimaging of α-particles," *Journal of Nuclear Medicine*, vol. 51, no. 10, pp. 1616–1623, 2010.

[4] F. Maskali, S. Poussier, P. Y. Marie, T. Nguyen, L. Antunes, P. Olivier, F. Plenat, S. Maîtrejean, F. Zannad, and G. Karcher, "High-resolution simultaneous imaging of SPECT, PET, and MRI tracers on histologic sections of myocardial infarction," *Journal of nuclear cardiology*, vol. 12, no. 2, pp. 229–230, 2005.

[5] H. Mizuma, M. Shukuri, T. Hayashi, Y. Watanabe, and H. Onoe, "Establishment of in vivo brain imaging method in conscious mice," *Journal of Nuclear Medicine*, vol. 51, no. 7, pp. 1068–1075, 2010.

[6] S. Yamada, R. Kubota, K. Kubota, K. Ishiwata, and T. Ido, "Localization of ^{18}F fluorodeoxyglucose in mouse brain neurons with micro-autoradiography," *Neuroscience letters*, vol. 120, no. 2, pp. 191–193, 1990.

[7] J. Cabello and K. Wells, "The spatial resolution of silicon-based electron detectors in β-autoradiography," *Physics in Medicine and Biology*, vol. 55, no. 6, pp. 1677–1699, 2010.

[8] E. Tribollet, J. J. Dreifuss, G. Charpak, W. Dominik, and N. Zaganidis, "Localization and quantitation of tritiated compounds in tissue sections with a gaseous detector of beta particles: comparison with film autoradiography." *Proceedings of the National Academy of Sciences*, vol. 88, no. 4, pp. 1466–1468, 1991.

[9] Y. Charon, P. Laniece, and H. Tricoire, "Radio-imaging for quantitative autoradiography in biology," *Nuclear medicine and biology*, vol. 25, no. 8, pp. 699–704, 1998.

[10] R. F. Johnston, S. C. Pickett, and D. L. Barker, "Autoradiography using storage phosphor technology," *Electrophoresis*, vol. 11, no. 5, pp. 355–360, 1990.

[11] J. Noguchi and K. Suzuki, "Imaging plate characteristics of positron emitters: ^{11}C, ^{13}N, ^{15}O, ^{18}F and ^{38}K," *Radiochimica Acta*, vol. 89, no. 7, pp. 433–438, 2001.

[12] G. Charpak, W. Dominik, J. P. Fabre, J. Gaudaen, F. Sauli, and M. Suzuki, "Studies of light emission by continuously sensitive avalanche chambers," in *Research On Particle Imaging Detectors*. World Scientific, 1995, pp. 61–67.

[13] N. Barthe, K. Chatti, P. Coulon, S. Maıtrejean, and B. Basse-Cathalinat, "Recent technologic developments on high-resolution beta imaging systems for quantitative autoradiography and double labeling applications," *Nuclear Instruments and Methods in Physics Research Section A: Accelerators, Spectrometers, Detectors and Associated Equipment*, vol. 527, no. 1-2, pp. 41–45, 2004.

[14] R. Ott, J. MacDonald, and K. Wells, "The performance of a CCD digital autoradiography imaging system," *Physics in Medicine and Biology*, vol. 45, no. 7, pp. 2011–2027, 2000.

[15] J. Cabello, A. Bailey, I. Kitchen, M. Prydderch, A. Clark, R. Turchetta, and K. Wells, "Digital autoradiography using room temperature CCD and CMOS imaging technology," *Physics in medicine and biology*, vol. 52, no. 16, pp. 4993–5011, 2007.

[16] G. Pratx, K. Chen, C. Sun, M. Axente, L. Sasportas, C. Carpenter, and L. Xing, "High-resolution radioluminescence microscopy of ^{18}F-FDG uptake by reconstructing the β-ionization track," *Journal of Nuclear Medicine*, vol. 54, no. 10, pp. 1841–1846, 2013.

[17] L. Chen, L. S. Gobar, N. G. Knowles, D. W. Wilson, and H. H. Barrett, "Direct charged-particle imaging system using an ultra-thin phosphor: physical characterization and dynamic applications," *IEEE transactions on nuclear science*, vol. 56, no. 5, pp. 2628–2635, 2009.

[18] P. Russo, A. Lauria, G. Mettivier, M. Montesi, M. Marotta, L. Aloj, and S. Lastoria, "^{18}F-FDG positron autoradiography with a particle counting silicon pixel detector," *Physics in Medicine and Biology*, vol. 53, no. 21, pp. 6227–6243, 2008.

[19] Q. Wang, J. Tous, Z. Liu, S. Ziegler, and K. Shi, "Evaluation of Timepix silicon detector for the detection of ^{18}F positrons," *Journal of Instrumentation*, vol. 9, no. 05, p. C05067, 2014.

[20] Q. Wang, Z. Liu, S. I. Ziegler, and K. Shi, "Enhancing spatial resolution of ^{18}F positron imaging with the Timepix detector by classification of primary fired pixels using support vector machine," *Physics in Medicine and Biology*, vol. 60, no. 13, pp. 5261–5278, 2015.

[21] I. Valin, C. Hu-Guo, J. Baudot, G. Bertolone, A. Besson, C. Colledani, G. Claus, A. Dorokhov, G. Dozière, W. Dulinski *et al.*, "A reticle size cmos pixel sensor dedicated to the STAR HFT," *Journal of Instrumentation*, vol. 7, no. 01, p. C01102, 2012.

[22] ICRU, "Stopping powers for electrons and positrons," *Report No. 37, International Commission on Radiation Units and Measurements, Bethesda, MD*, 1984.

[23] R. Rescigno, C. Finck, D. Juliani, E. Spiriti, J. Baudot, Z. Abou-Haidar, C. Agodi, M. A. G. Álvarez, T. Aumann, G. Battistoni *et al.*, "Performance of the reconstruction algorithms of the FIRST experiment pixel sensors vertex detector," *Nuclear Instruments and Methods in Physics Research Section A: Accelerators, Spectrometers, Detectors and Associated Equipment*, vol. 767, pp. 34–40, 2014.

[24] M. Bé, V. Chisté, C. Dulieu, E. Browne, V. Chechev, N. Kuzmenko, R. Helmer, A. Nichols, E. Schönfeld, and R. Dersch, "Table of radionuclides (vol. 1-a= 1 to 150)," *Bureau International des Poids et Mesures, France: Sèvres*, 2004.

[25] K. Hamacher, H. H. Coenen, and G. Stöcklin, "Efficient stereospecific synthesis of no-carrier-added 2-[18F]-fluoro-2-deoxy-D-glucose using aminopolyether supported nucleophilic substitution." *Journal of nuclear medicine: official publication, Society of Nuclear Medicine*, vol. 27, no. 2, pp. 235–238, 1986.

[26] S. Jan, C. Comtat, D. Strul, G. Santin, and R. Trebossen, "Monte Carlo simulation for the ECAT EXACT HR+ system using GATE," *Ieee transactions on nuclear science*, vol. 52, no. 3, pp. 627–633, 2005.

[27] T. N. Pham, C. Finck, P. Marchand, D. Brasse, F. Boisson, and P. Laquerriere, "^{18}F autoradiography using pixelated CMOS technology," in

2017 15th IEEE International New Circuits and Systems Conference (NEWCAS). IEEE, 2017, pp. 41–44.

[28] A. Lauria, G. Mettivier, M. C. Montesi, L. Aloj, S. Lastoria, M. Aurilio, and P. Russo, "Experimental study for an intraoperative probe for ^{18}F imaging with a silicon pixel detector," *Nuclear Instruments and Methods in Physics Research Section A: Accelerators, Spectrometers, Detectors and Associated Equipment*, vol. 576, no. 1, pp. 198–203, 2007.

[29] G. Deptuch, A. Besson, P. Rehak, M. Szelezniak, J. Wall, M. Winter, and Y. Zhu, "Direct electron imaging in electron microscopy with monolithic active pixel sensors," *Ultramicroscopy*, vol. 107, no. 8, pp. 674–684, 2007.

[30] S. Baechler, B. Masschaele, P. Cauwels, M. Dierick, J. Jolie, T. Materna, and W. Mondelaers, "The new cold neutron tomography set-up at SINQ," *Nuclear Instruments and Methods in Physics Research Section A: Accelerators, Spectrometers, Detectors and Associated Equipment*, vol. 481, no. 1-3, pp. 397–405, 2002.

[31] L. Katz and A. S. Penfold, "Range-energy relations for electrons and the determination of beta-ray end-point energies by absorption," *Reviews of Modern Physics*, vol. 24, no. 1, pp. 28–44, 1952.

[32] N. Barthe, S. Maîtrejean, and A. Cardona, "High-resolution beta imaging," in *Handbook of Radioactivity Analysis (Third Edition)*. Elsevier, 2012, pp. 1209–1242.

[33] J. Dupuis, C. Holst, and H. Kuhlmann, "Measuring leaf thickness with 3D close-up laser scanners: Possible or not?" *Journal of Imaging*, vol. 3, no. 2, pp. 22–36, 2017.

[34] F. Peyrin and J. M. Bonny, "Recalage d'images multimodales," *Le cahier des Techniques de l'Inra*, pp. 115–126, 2009.